

## Constitutive property of the local organization of leaf venation networks

S. Bohn,<sup>1</sup> B. Andreotti,<sup>1</sup> S. Douady,<sup>1</sup> J. Munzinger,<sup>2</sup> and Y. Couder<sup>1</sup>

<sup>1</sup>*Laboratoire de Physique Statistique de l'ENS, 24 rue Lhomond, 75231 Paris Cedex 05, France*

<sup>2</sup>*Institut de Systématique, Muséum National d'Histoire Naturelle, Laboratoire de Phanérogamie, 16 rue Buffon, 75005 Paris, France*

(Received 22 December 2001; published 28 June 2002)

The leaf venation of dicotyledons forms complex patterns. In spite of their large variety of morphologies these patterns have common features. They are formed of a hierarchy of structures, which are connected to form a reticulum. Excellent images of these patterns can be obtained from leaves from which the soft tissues have been removed. A numerical image processing has been developed, specially designed for a quantitative analysis of this type of network. It provides a precise characterization of its geometry. The resulting data reveals a surprising property of reticula's nodes: the angles between vein segments are very well defined and it is shown that they are directly related by the radii of the segments. The relation between radii and angles can be expressed very simply using a phenomenological analogy to mechanics. This local organization principle is universal; all leaf venation patterns studied show the same behavior. The results are compared with physical networks such as fracture arrays or soap froth in terms of hierarchy and reorganization.

DOI: 10.1103/PhysRevE.65.061914

PACS number(s): 87.90.+y, 05.65.+b, 89.75.Fb

### I. INTRODUCTION

The venation patterns of plant leaves have a great beauty, which results from the visual combination of their complexity and regularity. The pattern shown in Fig. 1(a) is the venous network of a dicotyledon leaf: *Gloeospermum sphaerocarpum*. This leaf was subjected to a chemical treatment to remove all the soft tissues, leaving only the veins. A vein, in fact, is more properly called a vascular bundle [1,2]. It is formed of three parts, each of them with a different function. At the core of these bundles are clusters of two distinct types of ducts. Xylem, which transports water from the roots to the tissues, and phloem, in which the chemical products synthesized in the leaf flows in the opposite direction towards the rest of the plant. These ducts are surrounded by a sheath of ground tissue made of lignin (wood). This sheath has a mechanical role in strengthening the rigidity of the leaf. What we observe is this sheath; its diameter is not necessarily proportional to the diameter of the ducts themselves.

#### A. Variability of the patterns

The patterns of different species exhibit a large variety of structures. For this reason, leaf venation has been investigated for its possible use in the systematic determination of species. Several attempts to classify the patterns were done, initiated by von Ettinghausen [3]. His classification was refined and completed by Hickey [4]. The more recent books by Klucking [5] give a systematic photographic record of a large number of venations and propose a different classification.

Until now, however, the venation has not been considered as a safe criterion for the systematic classification of plants because of its observed variability. When several leaves of the same plant are examined, they exhibit a common type of structure with still an individual pattern. This is the signature of the role of self-organization during the growth. This situation contrasts with, e.g., the venation pattern of dragonfly

wings, which are practically identical from one individual to another. In this latter case the pattern thus seems more directly determined by genetics. One aspect of this variability was investigated by Wylie [6,7] who demonstrated a dependence of the leaf thickness and the interveinal distances on the intensity of the exposure to the light.

#### B. The global structure of the vein pattern

In spite of the large variety of patterns observed in leaves, some properties are always present. Several features concerning the structure of the network can be noted.

(1) The hierarchy of the vein radii corresponds to a temporal order during the pattern formation [8,1]. The primary vein of the leaf in Fig. 1(a) is the central midvein. It is the largest and oldest. The secondary veins grow towards the leaf edge on either side of the midvein. The veins of third order are observed between the secondary ones. The higher orders are visible in Fig. 1(b). The veins become both thinner and shorter as their order increases. Approximately seven successive orders of veins can be identified in Fig. 1(b).

(2) The general pattern forms a reticulum. This means that, generally, all veins are connected at both their ends to the global array. For instance, each secondary vein is connected, at its base, to the primary vein and also by a loop to another secondary vein near the border. Similarly the tertiary veins usually connect two secondary veins. This feature is observed for all orders except the highest where the thinner veins (called the veinlets) are often left open ended. As a result the small scale structure of the array [shown on Fig. 1(b)] is formed by a juxtaposition of polygons called the areoles. All the open-ended veinlets are enclosed within these areoles.

In mature leaves the network morphology of the system leads to a redundancy in the flow paths, which is physiologically beneficial. If a vein is accidentally severed, the flow is not deeply perturbed because it bypasses the damaged region using the neighboring network. This is a very efficient process, as demonstrated by Wylie [7] and Magnasco [9].

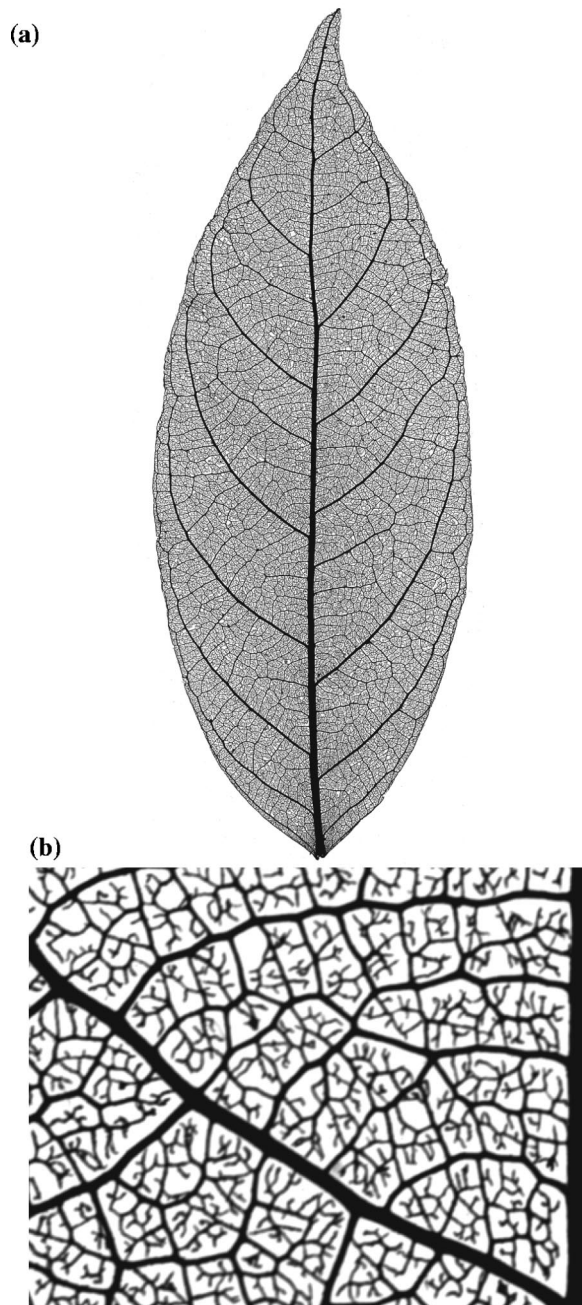


FIG. 1. The venation network of a dicotyledon (*Gloeospermum*) as it appears after a direct high-resolution scan. (a) The whole pattern (the leaf is 11.5 cm long). (b) A detail of the structure (0.75 mm $\times$ 0.59 mm).

### C. Global versus local geometric structure

The continuity of the veins within the above reported hierarchy provides an intuitive description of the venation pattern. However, in terms of strict definitions, this concept gives rise to fundamental problems requiring a specific investigation. The central vein, large at the base, becomes thinner and its radius in the tip region is often of the same magnitude as the radii of the small veinlets [Fig. 1(a)]. Furthermore, the histogram of radii of the vein segments (Fig. 7) is very smooth and does not give any indication to

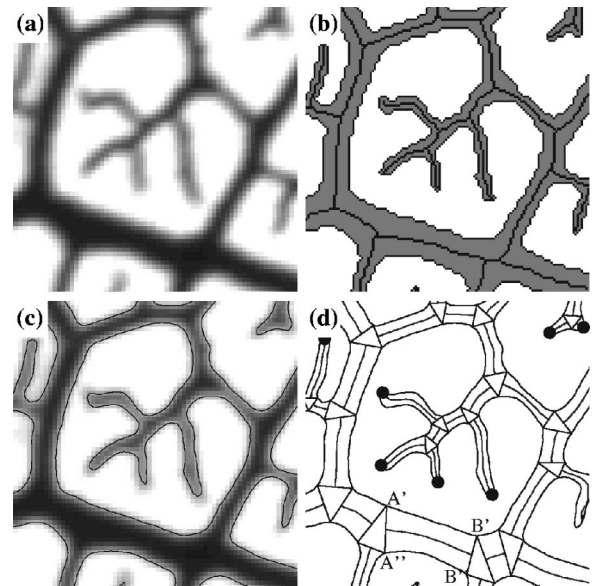


FIG. 2. Four steps of the image processing. (a) The leaf skeleton is scanned by a commercial scanner. (b) A new, binary image is built up. The gray points in this representation correspond to the black value points of the initial image, the black points between the gray and the white points are the borderlines and the black points in the middle of the gray regions are the results of the skeletonizing process. (c) Smooth borderlines are obtained using a linear interpolation. In this image they are projected on the scanned image. (d) The final aspect of the transformed image; nodes are represented by triangles and open ends by black disks. Between two nodes, a segment is defined by its two border lines and a middle line.

distinguish different generations. The classification of veins and generations simply based on the local radius, therefore, fails. Another problem is that many Y-shaped ramifications are observed at small scales [see Fig. 1(b)], where three segments of equal radii are connected by angles of  $120^\circ$ . Supposing that at such a Y ramification three distinct veins are connected, will result in defining an unrealistic number of veins and generations. If we suppose, on the other hand, that all three branches of the Y belong to the same vein, too many segments are stuck together and netlike veins are formed. In short, it is often not easy to define an objective criterion by which to decide where a vein starts and where it ends.

These problems can be avoided by focusing on the local geometric structure. The concept proposed here and used in the following text is simple and can be used for networks of very different natures. In contrast to the description based on continuous veins of different orders, which can be seen as a global approach, this concept allows analysis of the local structure. We consider the venation pattern as a set of nodes, segments and free endings. A node connects at least three segments in the same way as a crossroad connects at least three parts of street. A segment is the link between two nodes or between a node and a free ending. It can be compared to a segment of street which links two crossroads or a crossroad and a dead end. This is shown in Fig. 2(d). The nodes are represented by triangles, the free endings by black disks. Two border lines and a middle line form a segment. Different properties are assigned to nodes and segments. Each segment

has a defined length and radius, both measured in the image processing. At a node three angles between the segments are determined. While this representation allows for a systematic analysis, the concept of veins and hierarchy is kept in mind to interpret the obtained results.

In this study we focus on the angles between vein segments to characterize the geometry of the pattern. This choice permits comparison of the venation so as to better understand physical reticula. This is dealt with in the conclusion.

## II. IMAGE PROCESSING AND STATISTICAL TECHNIQUES

### A. Image acquisition and processing

In the case of *Griffonia simplicifolia*, the skeletons were obtained from fresh leaves of plants in culture, which were naturally cleaned by unidentified animals (among which are the larvae of *Platyhelminthes*). For all the other species the skeletons were obtained from leaves collected on dry plants of the herbarium of the Laboratoire de Phanérogamie, MNHN (P). They were put in 10% sodium hydroxide solution at 70–80 °C until the epidermis unstuck. Then for both materials, the epidermis and mesophyll were removed by fine grips and writing brush. The skeletons were then bleached in 10% hydrogen peroxide for 30–60 min, washed thoroughly in water, stained in 10% Fuchsine for 2 h, washed, dried, and conserved in crystal paper.

The leaf skeletons were then scanned directly using a commercial scanner in transmission mode with a resolution of 2000 pixels/inch and 256 gray values. Figure 1(a) shows the type of resulting image. As can be seen in Fig. 1(b), the whole structure, including the highest order veins, is well resolved. We want to treat this image so as to obtain relevant data on the pattern. We thus need to extract all the information about the topological structure (connections, areoles), the segments (length, diameter), and the nodes (angles). Since we want to obtain statistically relevant data, it is necessary to develop a numerical process for imaging a whole leaf.

In Fig. 2 the different steps of this treatment are demonstrated for the detail in Fig. 1. The initial image [Fig. 2(a)] is strongly contrasted with dark veins on a light background. In the first step, a gray threshold is imposed and the image is decomposed in white (gray values smaller than the threshold) and black areas. This is done in the following way. A new image of double size is created by the mask shown in Fig. 3. The value of a point with coordinates  $(2i, 2k)$  of the new image is white ( $w$ ) if the gray value of the corresponding point of the original image  $(i, k)$  is smaller than the threshold; otherwise it is black ( $b$ ). The values of the inserted points are defined by the neighborhood. They have the black value if the new point is located between two black points ( $b$ ) and the white value ( $w$ ) if the new point is located between two white points ( $w$ ). The points with a white and a black neighbor define the borderline of black and white. These borderline points [called ( $t$ ) for threshold] in Fig. 3 are enumerated and an exact position is calculated by comparing the linear interpolation of the gray values of the neighboring

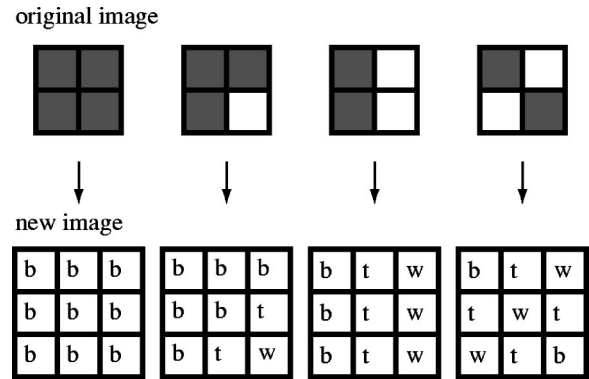


FIG. 3. The principle used to apply the threshold and to decompose the image into black ( $b$ ) and white ( $w$ ) areas. The borderline points are represented by ( $t$ ). In the alternating situation (at the right) the value of the center point of the new image is ( $w$ ). In this way we obtain distinct ( $b$ ) areas and each ( $t$ ) point can be unequivocally assigned to one ( $b$ ) area.

points with the imposed threshold. The results are shown in Figs. 2(b) and 2(c): in Fig. 2(b) the ( $w$ ) areas are drawn in white and the ( $b$ ) areas in gray. The black points separating these areas form the border line. Figure 2(c) shows these border lines, which are stored in memory as a series of real value vectors, projected onto the original image. They are smoother than those obtained by direct application of a threshold [Fig. 2(b)] and thereby discretization effects are avoided.

The second step consists in detecting the topology of the network. To do this, the ( $b$ )-value areas are shrunk from the border line to simple lines shown as black lines in Fig. 2(b). Deviating from the standard skeletonizing technique, the “history” of the shrinking process is kept in memory so that for each point of a central line, we are able to find the two corresponding points on the border lines from where the shrinking process has started. On these simple central lines the nodes (points with at least three neighbors) and the free endings (points with only one neighbor) are detected; the information about the connection of a node with its three neighbors is obtained as well. As the history of the shrinking process is stored in memory, a node is not a point but a triangular zone and two neighboring nodes are connected by the two border lines [ $A'B'$  and  $A''B''$  in Fig. 2(d)]. All measurement procedures are based on these triangles and border lines.

The measurement procedures used on the set of nodes and border lines are demonstrated in Fig. 4. In order to define the triangle representing a node [Fig. 4(a)] we choose three points  $a, b, c$  on the three borders surrounding the node. We slide them on these borders until we obtain the three points  $A, B, C$  forming the triangle with a minimal perimeter. As the area of this triangle belongs to the all three segments, neither lengths nor radii nor angles have any meaning in these regions. The two border lines and the two triangles enclose a quadrangular region, the area ( $A$ ) of which can be computed directly. Then, starting from one side of a node triangle, we can move in parallel on the two border lines, until we reach

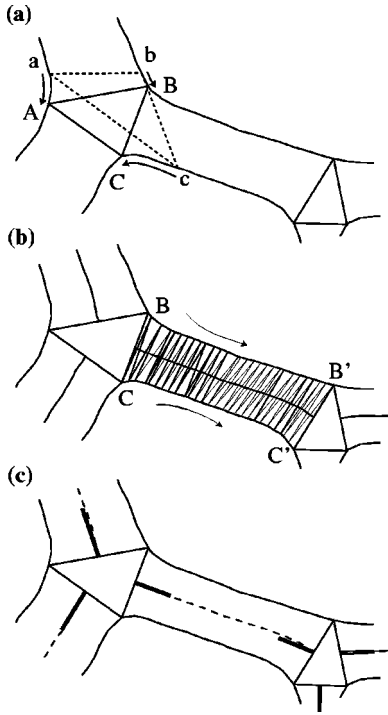


FIG. 4. The three steps for the definition of the geometric characteristics of the pattern. (a) Nodes: The triangle ( $abc$ ) representing the node is changed by shifting the apices on the border line in order to minimize its perimeter. ( $ABC$ ) is the minimized triangle. (b) Segments: The area  $A$  of the segment is defined as the area enclosed by the lines connecting the points ( $BCC'B'$ ). The middle line is obtained by simultaneously moving from  $B$  to  $B'$  and from  $C$  to  $C'$  on the two border lines (arrows), and by calculating at each step the middle of the line between the lines  $BB'$  and  $CC'$ . The length and the radius of the segment are calculated during this “wrapping process.” (c) Angles: On a length of the order of the triangle side, the extremities of the middle lines are fitted by straight lines. Note that each node connects three segments having a large width ( $L$ ), an intermediate width ( $I$ ), and a small width ( $S$ ), respectively.

the next triangle. For each step there is a small line that links the two border lines and by calculating its center a new, smoother middle line is obtained [Fig. 4(b)]. The length  $L$  of this line is computed and the characteristic value for the segment’s radius is defined by  $R=A/2L$ .

At each node, each of the segments is replaced by a straight line that is the best fit of the middle line starting from the side of the triangle with a length equal to this side of the triangle [Fig. 4(c)]. These straight lines define the absolute directions of the segments at the node and, therefore, the angles. When two nodes are very close to each other, the length of the middle line separating the two triangles is smaller than the fitting length. In such cases the two triangles are pasted together and nodes with four or more segments are formed. These nodes are ignored in the following. They should be treated separately in the statistics.

### B. Statistical analysis: The geometrical constraints in a two-dimensional network

Since the analyzed leaves are flat, we will consider their venation patterns as two dimensional. Since we are going to

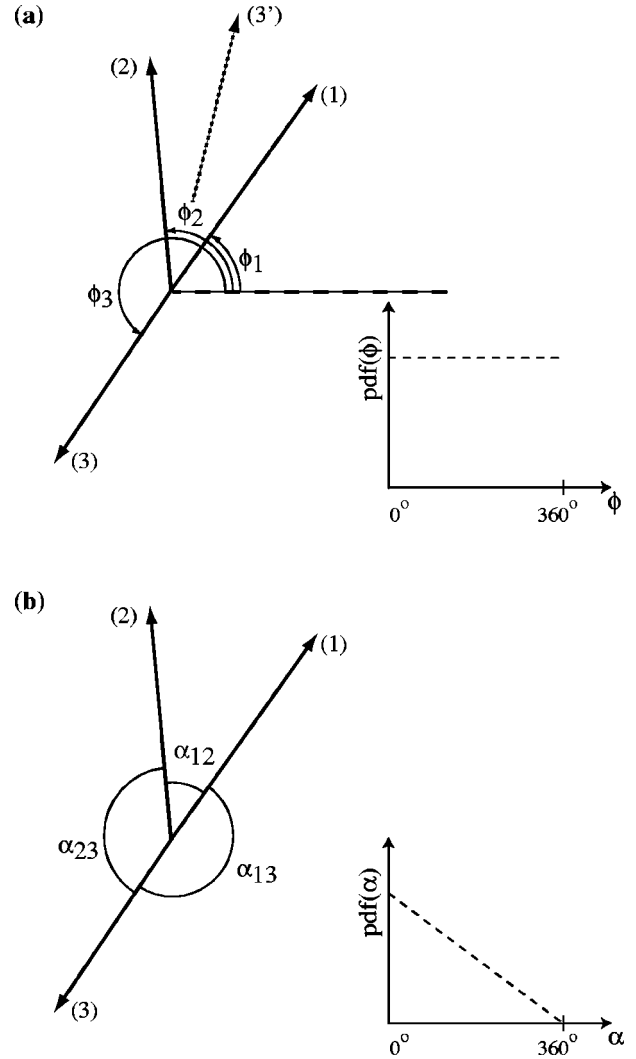


FIG. 5. Sketch defining the absolute angles  $\phi_i$  (a) and the relative angles  $\alpha_{lk}$  (b) at a node. When the three absolute angles are chosen at random the resulting pdf [ $p(\phi)$  is constant in inset (a)] and the corresponding  $p(\alpha)$  [inset (b)] are proportional to  $(360^\circ - \alpha_{12})$ .

analyze statistical results on the distribution of angles at a node, we first have to examine their behavior in the case of a random array. The Euclidean geometry requires the sum of all angles between segments at a node to be  $360^\circ$ . To analyze the angle data we have to understand the action of this constraint on the statistics.

Let us consider the case where the directions of the three segments at a node are chosen randomly and isotropically. We consider a node [Fig. 5(a)] and first define the position of the segments by their angle  $\phi_i$  with a fixed direction  $Ox$ . For each of the three segments, the probability that it is oriented in the absolute direction  $\phi_i$  is independent of  $\phi_j$ . As a result, the probability density function  $p_{ran}(\phi_i)$  (where the index “ran” stands for random) is a constant [Fig. 5(a) inset] and the probability that  $\phi_i$  is contained in an interval  $[a, b]$ ,  $P(a \leq \phi_i \leq b)$ , is proportional to the length of the interval. We are now interested in the angles  $\alpha_{kl}$  formed, at a node by two segments  $k$  and  $l$  (Fig. 5 inset). The probability density function (pdf) of these angles is less trivial.

We first consider two segments 1 and 2 being placed in random directions  $\phi_1$  and  $\phi_2$ , respectively. If no order is used they form two angles  $(\phi_2 - \phi_1)$  or  $[360^\circ - (\phi_2 - \phi_1)]$ . One of these angles is  $\alpha_{12} \leq 180^\circ$  and the other  $\alpha_{12} \geq 180^\circ$ . The value that will actually be measured depends on the position of the third segment. If it is placed in a random direction it has a greater probability of being between 1 and 2 on the side of the larger angle. As a result, the chosen  $\alpha_{12}$  has a greater probability of being the smaller of the two possible values. To simplify the argument we assume that  $\phi_1 = 0$ , e.g., the coordinate system is chosen so that the fixed direction  $Ox$  is identical to the direction  $\phi_1$ . The probability of obtaining an angle  $\alpha_{12}$  is the sum of the two probabilities,

$$p_{ran}(\alpha_{12}) = P(\phi_2 = \alpha_{12})P(\phi_3 > \alpha_{12}) \\ + P(\phi_1 = \alpha_{12})P(\phi_3 < 360^\circ - \alpha_{12}).$$

As  $P(\phi_2 = \alpha_{12}) = P[\phi_2 = (360^\circ - \alpha_{12})]$  are constant and as  $P(\phi_3 > \alpha_{12}) = P[\phi_3 < (360^\circ - \alpha_{12})] \propto (360^\circ - \alpha_{12})$ , the resulting pdf is

$$p_{ran}(\alpha_{12}) \propto (360^\circ - \alpha_{12}). \quad (1)$$

This probability  $p_{ran}(\alpha_{12})$  is given in Fig. 5(b) (inset). In the following, using the image processing we obtain experimental probability density functions  $p_{exp}(\alpha_{12})$ . In order to eliminate from our results the effect of the geometrical constraint, all the pdfs that will be shown below are the measured histograms rescaled by the random value.

$$p(\alpha_{12}) = \frac{p_{exp}(\alpha_{12})}{p_{ran}(\alpha_{12})}. \quad (2)$$

Note that if there were no irregularities and if the angles were really randomly distributed the resulting histogram  $p(\alpha_{12})$  would be constant.

### III. ANGLE DATA

#### A. Global pdf for the vein radii and angles

The results presented here were obtained using a *Gloeospermum* leaf of the type shown in Fig. 1. For a given leaf the venation pattern is composed of several thousand nodes [73 526 are detected in Fig. 1(a)] and free endings (46 124) with thousands of segments (127 610). 10 181 simple nodes with three segments are collapsed because the fitting length was shorter than the segment (see above) so that for this leaf the statistics were done on 63 345 nodes with three segments.

Figure 6 shows the histogram of  $p(\alpha)$  in this case. It can be immediately seen that the network is not random, since the angles between vein segments are found to have values mostly between  $90^\circ$  and  $180^\circ$ . Furthermore, the pdf seems to have two ill-defined maxima. Similar results were obtained in all the leaves we analyzed, as will be discussed below.

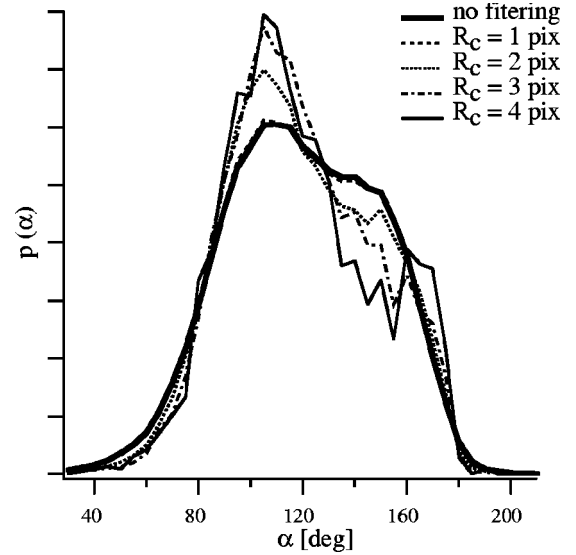


FIG. 6. The normalized pdf  $p(\alpha)$  for all the nodes of a leaf of *Gloeospermum*. The bold line shows the complete histogram, the others are histograms obtained on filtered patterns with different values of the radius threshold  $R_c$  (1 pixel =  $12.5 \mu\text{m}$ ).

We must note that for a very small number of nodes (much less than 1%) the automatic treatment fails and the measured angles are close to  $360^\circ$ . Due to the renormalization by  $p_{ran}$  these points become important when mean values are calculated. To avoid this artifact, all the points corresponding to values of  $\alpha$  larger than  $300^\circ$  have been removed.

The visual impression given by Fig. 1 suggests that the structure is more isotropic at small scales than at large scales. For this reason we investigated whether or not the angle distributions depended on the vein sizes. Figure 7 is the histogram of the width of all the segments of the patterns. It is dominated by the small scales. Using the measured thickness of the veins, we could create “filtered patterns” from which all segments with a radius smaller than an imposed threshold

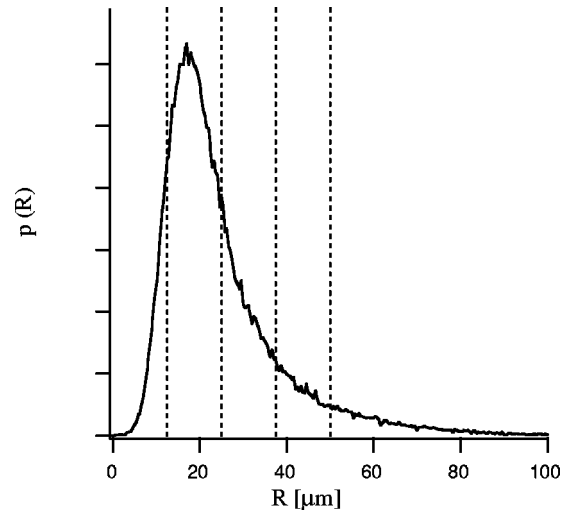


FIG. 7. The histogram of the radii of the segments. The vertical lines are the threshold radii used in the filtering process (see Fig. 8).

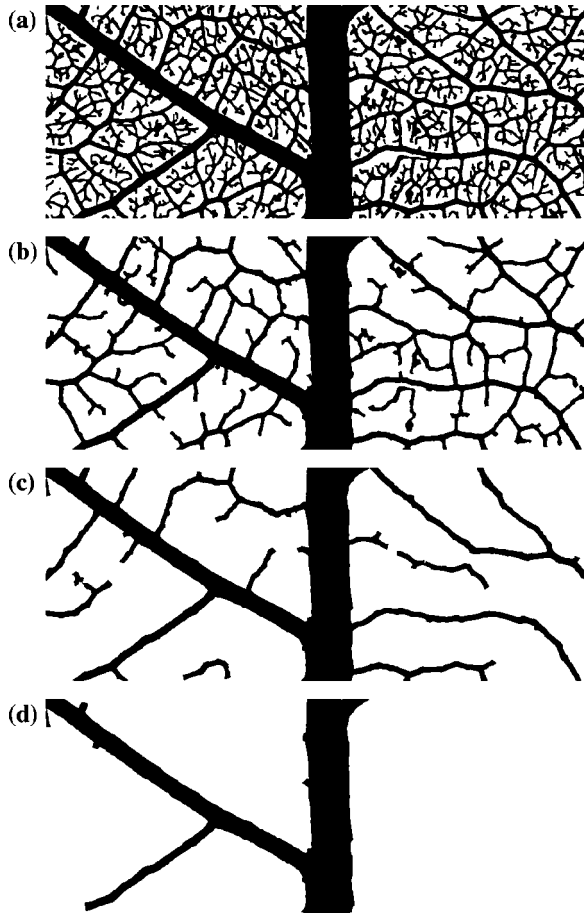


FIG. 8. Details of the *Gloeospermum* leaf after filtering with different threshold radii; (a) without filtering, (b)  $R_c = 25 \mu\text{m}$ , (c)  $R_c = 37.5 \mu\text{m}$ , and (d)  $R_c = 50 \mu\text{m}$ .

$R_c$  were removed. Figure 8 shows details of the resulting networks for three different values of the threshold. New histograms are computed on the filtered network, and are plotted in Fig. 6. In the absence of filtering, the thin veins dominate the statistics. The pdfs do not change in shape but the two maxima are slightly better resolved. There does not seem to be a strong dependence of the angle distribution on the global size of the veins. The fact that the maxima become sharper will be understood in the context of the results given in the following paragraph.

### B. Conditioned pdfs for the angles

Up to now, no distinction has been made between the three angles of a given node. However, it is clear that most nodes are the meeting points of veins having different diameters. In the following, before building up histograms, we will, at each node, distinguish the three segments by their radii. They are labeled large ( $L$ ), intermediate ( $I$ ), and small ( $S$ ). We will then measure three angles. The first one,  $\alpha_{LI}$ , is the angle between the segments of largest and intermediate radii,  $\alpha_{IS}$  is the angle between the segments of intermediate and smallest radii, and  $\alpha_{LS}$  is the angle between the segments of largest and smallest radii.

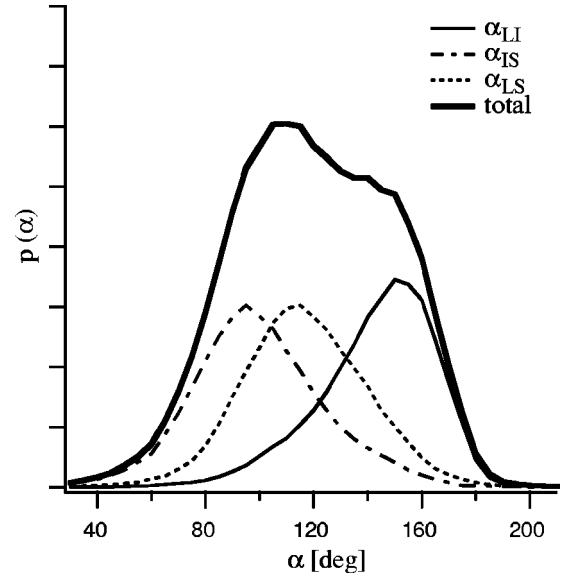


FIG. 9. The normalized pdf  $p(\alpha)$  for a leaf of *Gloeospermum* and its decomposition into three pdfs  $p(\alpha_{LI})$ ,  $p(\alpha_{IS})$ , and  $p(\alpha_{LS})$ , in which the relative radii of the segments have been taken into account.

The pdfs  $p(\alpha_{LI})$ ,  $p(\alpha_{IS})$ , and  $p(\alpha_{LS})$  shown in Fig. 9 are much simpler; each of them has only one maximum and the three maxima are different. The double maximum of the total histogram is, therefore, a result of the superposition of these three simpler histograms. The values of the three angles of a node are thus directly related to the local hierarchy of the meeting vein sizes.

In order to quantify this local hierarchy we use as a parameter  $R_S/R_L$ , the ratio of the radius of the thin segment to that of the thick one. The radius of the segment of intermediate size is usually close to the large one and, therefore, the configuration of radii is well defined by the chosen parameter (see Fig. 10). For  $R_S/R_L$  close to 1 all radii are nearly equal and no hierarchy can be defined. For  $R_S/R_L$  close to 0, a thin vein is connected to a thick one. Figure 11 shows the normalized histogram of  $R_S/R_L$ . It has a maximum at about 0.5, which means that intermediate situations are frequent.

Figure 12(a) shows a set of conditioned histograms  $p(\alpha_{LI})$  for the angle between the thick and intermediate veins. Each single histogram is obtained by taking into account only the nodes where  $R_S/R_L$  is in a chosen range of values. The original histogram is thus decomposed in sharper, more symmetrical histograms. For  $R_S/R_L$  close to 1 the three veins have approximately the same size and the symmetry of the situation is reflected in the symmetry of the angles that are all approximately equal to  $120^\circ$ . For very small values of  $R_S/R_L$ , a very thin vein is only a small perturbation to the thick vein and the angle  $\alpha_{LI}$  is close to  $180^\circ$ . Between the two extreme situations the angles of the peak vary continuously.

The dependency of the pdfs  $p(\alpha_{IS})$  and  $p(\alpha_{LS})$  [Figs. 12(b) and 12(c)] on the ratio  $R_S/R_L$  is much weaker. The mean value of  $\alpha_{IS}$  is about  $100^\circ$  for small  $R_S/R_L$  and rises to the symmetric  $120^\circ$  for  $R_S/R_L$  close to 1.  $p(\alpha_{LS})$  stays remarkably constant. Its mean value and its maximum

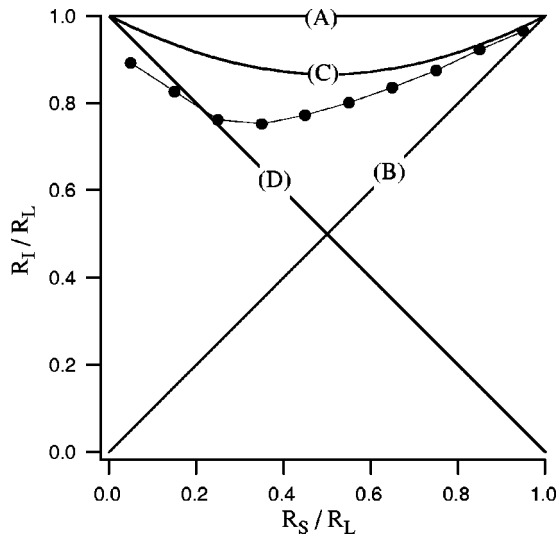


FIG. 10. The averaged values of  $R_I/R_L$  as a function of  $R_S/R_L$  (black disks). Lines (A) and (B) are the limits imposed by the definition, lines (C) and (D) are explained in Sec. V.

are both close to  $120^\circ$ . The pdfs  $p(\alpha_{IS})$  and  $p(\alpha_{LS})$  stay quite large. Note that the small veins still dominate the statistics. Either we have a small vein connected to a large one, or three small segments are linked together. The number of nodes with three large segments is so small that these configurations have no influence on the statistical results. But nevertheless, comparing the results with Fig. 1, the same behavior can be seen in configurations with large segments, too.

The results can, therefore, be interpreted as the perturbation of a larger, older vein by a younger and smaller vein that connects to it. The difference between  $\alpha_{LI}$  and  $180^\circ$  is a measure of this perturbation. It is a function of the ratio of the radii of the two veins. If the older vein is much larger than the younger one, the perturbation is minor and the vein remains straight. With increasing  $R_S/R_L$  the perturbation be-

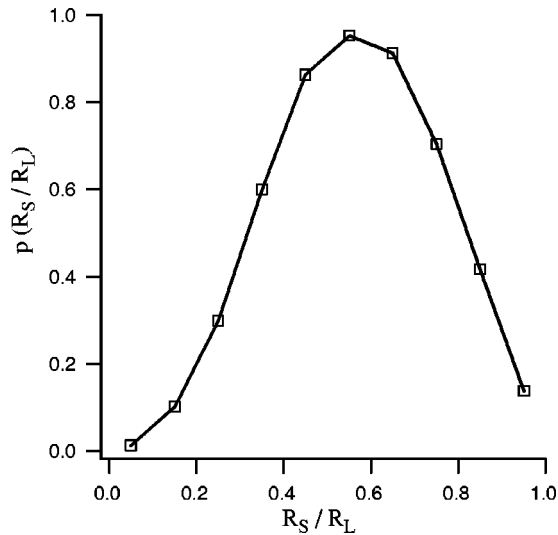


FIG. 11. The number of nodes as a function of their values of  $R_S/R_L$  (normalized): intermediate situations are frequent.

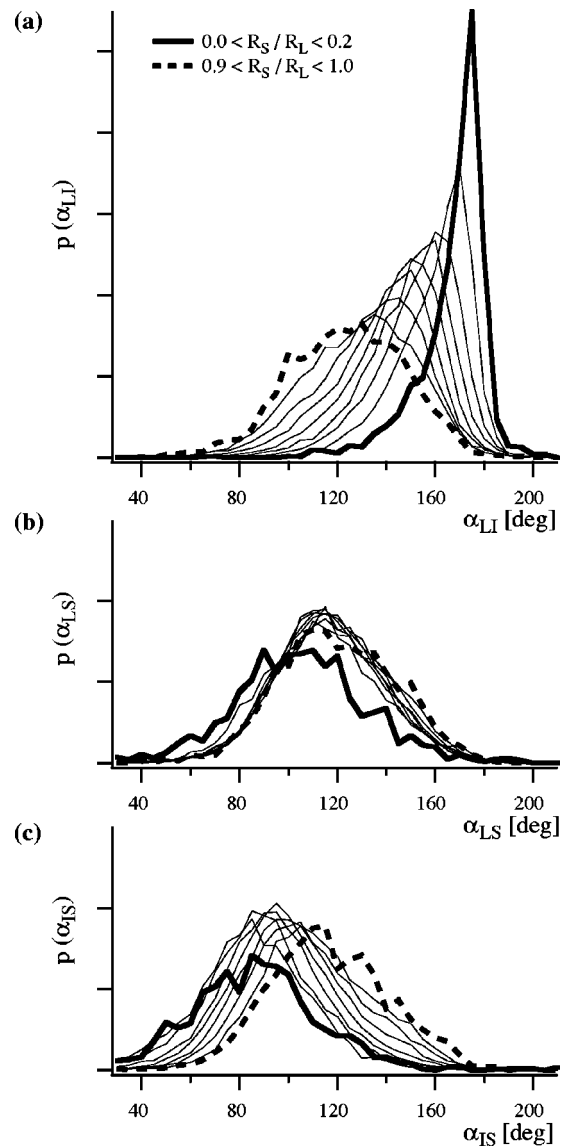


FIG. 12. (a) The decomposition of the pdfs  $p(\alpha_{LI})$  [shown in (a)],  $p(\alpha_{IS})$  [in (b)], and  $p(\alpha_{LS})$  [in (c)]. Each node is characterized by its ratio of radii  $R_S/R_L$ . Each pdf is obtained by limiting the analysis to nodes with  $R_S/R_L$  in a fixed interval. As  $0 \leq R_S/R_L \leq 1$ , nine distinct intervals have been defined. The bold lines are the normalized pdfs for small values of  $R_S/R_L$ , the bold, dashed lines are the normalized pdfs for large values of  $R_S/R_L$ .

comes stronger and stronger, the old vein seems to be pulled by the smaller one. The  $120^\circ$  angles for  $R_S/R_L$  close to 1 result from the mutual perturbation of the three segments: the width of the histograms of  $p(\alpha_{IS})$  and  $p(\alpha_{LS})$  indicates that the orientation of the small vein is less well determined.

### C. Comparison to other specimens

Specimen of the leaves of six other dicotyledons, *Amphirhox longifolia*, *Griffonia simplicifolia*, *Hybanthus caledonicus*, *Melicytus macrophyllus*, *Rinorea amapensis*, and *Leonia crassa*, were analyzed in a similar way. Figure 13 shows details of the photos of these six leaves together with a detail of the already discussed *Gloeospermum* leaf. Although the

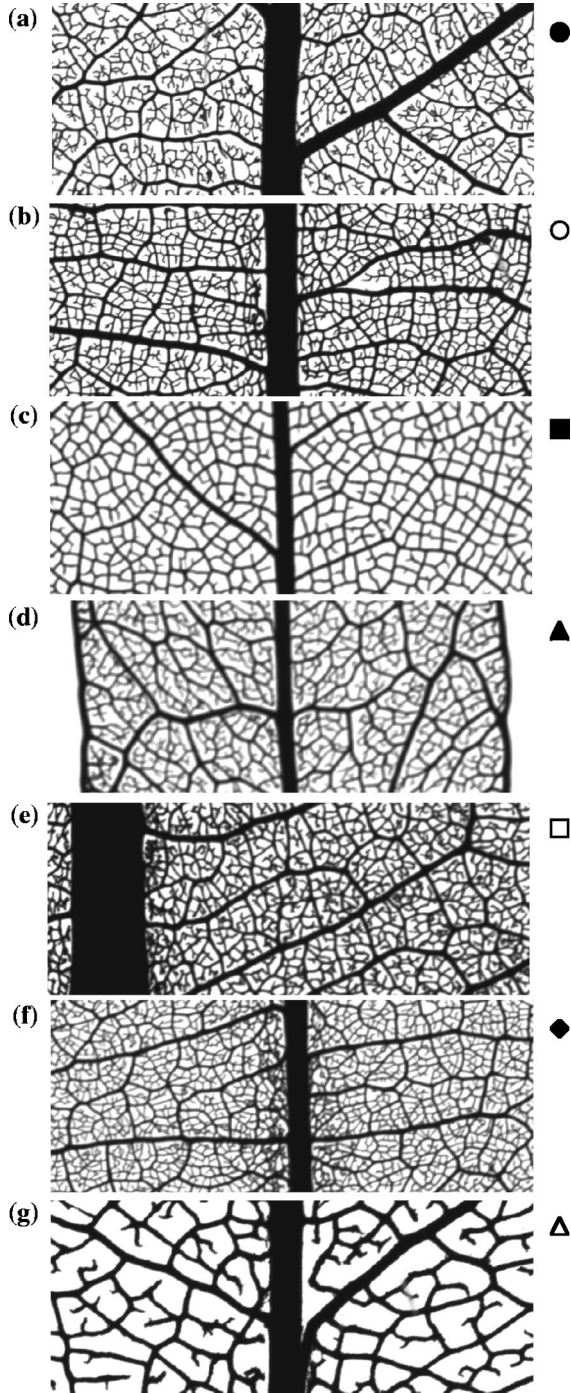


FIG. 13. Details of the seven venation patterns of leaves of various dicotyledons at the same scale; (a) *Gloeospermum sphaerocarpaceum*, (b) *Amphirrhox longifolia*, (c) *Griffonia*, (d) *Hybanthus Caledonicus*, (e) *Melicytus macrophyllus*, (f) *Rinorca amapensis*, and (g) *Leonia crassa*. The height of each is 3.9 mm. Although six of these leaves belong to the same family, their networks differ in the distribution of the radii, the number of free ending veinlets, and the characteristic length scale. The symbols used in Figs. 14 and 17 are indicated on the right of each image.

seven species are close to each other in evolution (six of them are part of the same family of *Violaceae* [10]) their venation patterns show a large variety. If we consider such

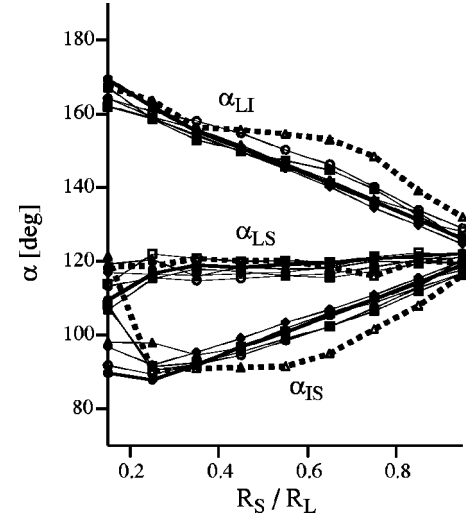


FIG. 14. The averages of the three angles  $\alpha_{LI}$ ,  $\alpha_{IS}$ , and  $\alpha_{LS}$  as a function of  $R_S/R_L$  for the seven specimens. The legend to identify the different leaves is given in Fig. 13. The bold line is for *Gloeospermum*. Note that they show identical behavior. The slightly different one is *Melicytus* (dashed line).

characteristics as the interveinal distances, the number of free ending veinlets, or the size hierarchy of the veins, we find the networks to be very different from one another.

In spite of these differences, the results of the analysis of the angles show the same properties as those for the *Gloeospermum* leaf. Figure 14 collects the averages of the three angles depending on  $R_S/R_L$  for the seven leaves studied. Surprisingly, only small interspecies variation can be observed. Nevertheless, the local dependency on the relative scale and the invariance on an absolute scale are mainly the same for all leaves. The relation between angles and radii is, therefore, much more general than we expected. This universality seems to be an organization law of the venation pattern, and we are, therefore, not able to distinguish the different species by the angle pdfs. Other properties, for example, the area of the areoles, the number of veinlets, and the radii of the veins, seem to be more appropriate quantities for systematic botany.

## IV. MODELING

### A. The “force model”

The previous results lead to the so called force model (Fig. 15). We imagine that each segment pulls on a node with a force in the direction of the segment. Its magnitude is an increasing function of the radius of the segment. In the equilibrium state the sum of the three forces has to be zero:

$$0 = \mathbf{F}_1(R_1) + \mathbf{F}_2(R_2) + \mathbf{F}_3(R_3), \quad (3)$$

$$0 = F(R_1)\mathbf{e}_{\phi_1} + F(R_2)\mathbf{e}_{\phi_2} + F(R_3)\mathbf{e}_{\phi_3}. \quad (4)$$

The directions  $\phi_i$ , and with them the angles, are determined by the three radii. For three segments of equal radii the resulting angles are  $120^\circ$  and for a very thin segment and two thick segments, the angle between the two thick seg-

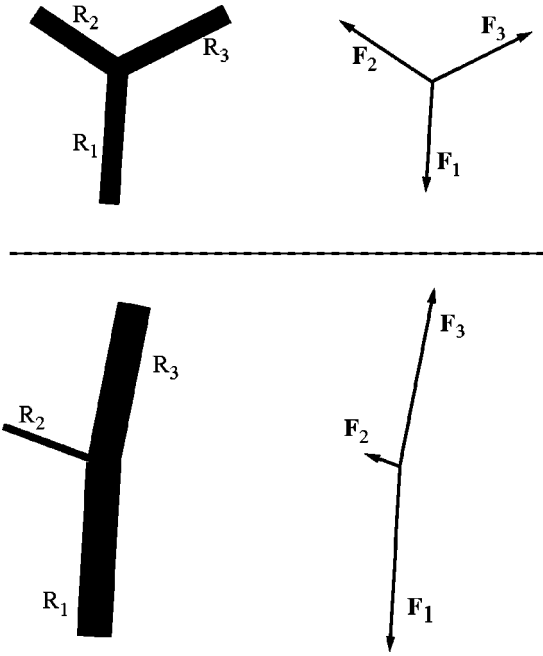


FIG. 15. Illustration of the so-called force model. Each segment is replaced by a force depending on its radius. The angles between the three segments result from the mechanical equilibrium.

ments will be close to the  $180^\circ$ . Qualitatively, this description agrees with the experimental results and allows the understanding of the intermediate situations.

The condition (4) is equivalent to

$$F(R_i)\sin\alpha_{ik}=F(R_l)\sin\alpha_{lk}. \quad (5)$$

To find the function  $F(R)$  that matches the experimental results, the functional

$$\Xi[F(R)]=\sum_{\text{all nodes}}\sum_k\frac{[F(R_i)\sin\alpha_{ik}-F(R_l)\sin\alpha_{lk}]^2}{F(R_k)^2+F(R_l)^2} \quad (6)$$

has been minimized numerically. The denominator is an estimation of the error. The obtained force functions are plotted in Fig. 16 for the seven leaves. The force can by definition be given in arbitrary units. For all seven leaves it increases linearly with the radius. This is in agreement with the absence of an absolute scale in the angle data (see Fig. 6). We can note that this well defined result differs from what would be obtained in the interaction of cylindrical elastic segments. In this latter case a quadratic dependency of the force on the radius would be expected. The linear dependency corresponds to an interaction of the elastic tubes.

### B. Comparison with the measurements

The best test of the force model consists in taking the whole data, removing the measured angles, taking the fitted force function and calculating the angles based on the force model. After this the histograms can be plotted and compared to the measured histograms. Figure 17 is of the same nature as Fig. 14, but here the angles are calculated.

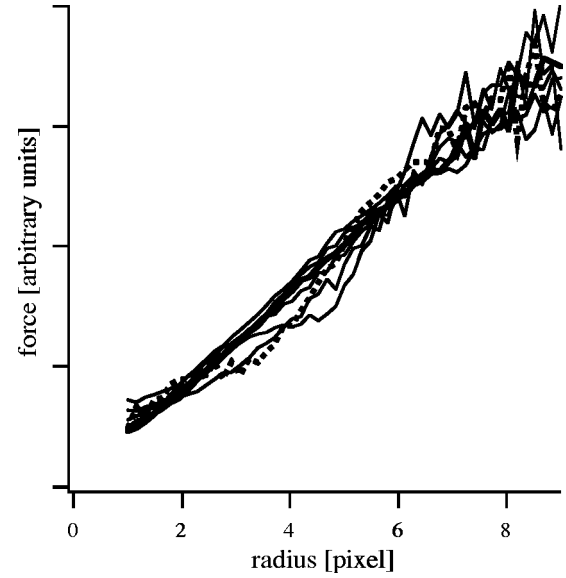


FIG. 16. The calculated functions  $F(R)$  for the seven leaves. The strength of the “force” in the force model is almost linear to the radius.

For the angles  $\alpha_{LL}$  the calculation matches perfectly with the experimental results. For the two other angles the calculated values show qualitatively the same behavior as the experimental values, but for small  $R_S/R_L$  there is a quantitative deviation. This may result from the fact that for such nodes the direction of the small segments is very sensitive to slight changes in the radii of the thick segments. The nonperfect overlap of experimental and theoretical values may, therefore, have its origin in the nonperfect accuracy of the determination of the radii. Note that in both figures, Figs. 14 and 17, the *Melicytos* leaf differs slightly from the others. The measured differences are reproduced by the calculation.

Assuming the linear dependency of the force on the radius, the reported results can be expressed in a simple geo-

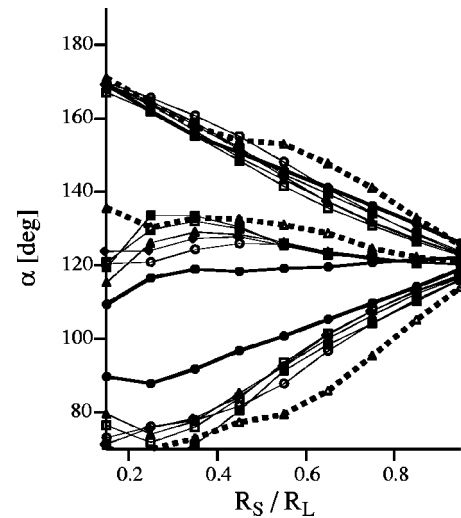


FIG. 17. Same as Fig. 14, but with the angles calculated by the force model. The calculations reproduce the measurements well. Note that, as in Fig. 14, the *Melicytos* (dashed line) is slightly different.

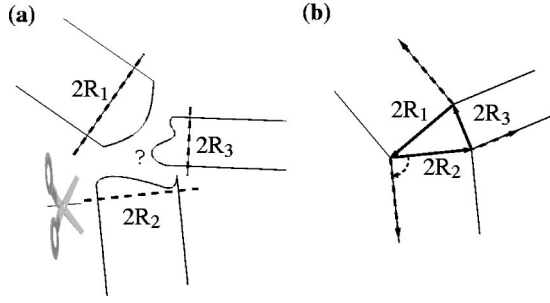


FIG. 18. Construction of the angles between three segments: cut the three segments at right angles. Assemble them so that the cuts form a triangle.

metric way shown in Fig. 18. After building up the equilibrium force triangle with forces having magnitudes proportional to the segment diameter, each force is rotated by  $90^\circ$  (an operation that does not change the relative angles). The directions of the segments are given by the directions of the forces. The former are, therefore, directly obtained by cutting each segment at right angles [Fig. 18(a)] and reassembling them so as to form a triangle with the cuts [Fig. 18(b)].

The force triangles in (Fig. 18) are very similar to the triangles representing the nodes [Fig. 2(d)]. This fact is not trivial. The image processing has also been tested on fracture arrays. In this case, the force model does not match the angle data. The description developed here is, therefore, characteristic for the venation patterns.

## V. RELATION BETWEEN THE RADII OF THE THREE SEGMENTS

Radii and angles have been defined as local properties, ignoring the intuitive continuity of veins of a given age and size. This concept of nodes and segments allows us to correlate radii and angles. The relation between these, compactly described by the so-called force model, can be seen as a constitutive relation of the local organization of the pattern. The angles are determined by the three radii, or more precisely, by the ratios  $R_S/R_L$  and  $R_I/R_L$ . The relation between the three radii is not trivial: the coexistence of nodes with three segments with equal radii, and nodes with two large segments and a thin one, do not allow a relation of the form

$$R_I^\gamma = R_2^\gamma + R_3^\gamma, \quad (7)$$

which would be expected by flow conservation considerations.

The choice of the ratio  $R_S/R_L$  as a parameter to define a node can be justified by a discussion of the results displayed in Fig. 10. At a given node the intermediate and the large radii are usually close to each other. Direct observation of the pattern shows that the corresponding segments belong to the same vein on which a vein of smaller diameter is connected. If the larger vein was of constant diameter, there would be equality of  $R_I$  and  $R_L$  and the representative points would be located on line (A) in Fig. 10. The measured data do not confirm this hypothesis exactly. For  $R_S/R_L$  close to 1 the

intermediate radius  $R_I$  is by definition close to  $R_L$ . For  $R_S/R_L$  close to 0, the small radius is much smaller than the large one, the measured intermediate radius is actually close to the large one. But in general the ratio  $R_M/R_L$  is not constant and equal to 1: the plot of  $R_M/R_L$  as a function of  $R_S/R_L$  shows a minimum at  $R_S/R_L=0.5$ . This characteristic can be recovered from the data on the angle distribution, using the force model. It is observed (Figs. 12 and 14) that the angle between the large and the small segment  $\alpha_{LS}$  stays constant at  $120^\circ$ . The construction of Fig. 18 and simple trigonometry leads to

$$R_I^2 = R_S^2 + R_L^2 - 2R_S R_L \cos(180^\circ - \alpha_{LS}). \quad (8)$$

With  $\alpha_{LS} = 120^\circ$  we obtain in terms of the ratios

$$\frac{R_I}{R_L} = \sqrt{1 - \frac{R_S}{R_L} + \left(\frac{R_S}{R_L}\right)^2}. \quad (9)$$

Line (C) in Fig. 10 is the plot of this function. Qualitatively this is in agreement with the measured data. The constant  $120^\circ$  angle is, therefore, the direct consequence of the differences between the intermediate and the large radii.

If one radius is larger than the sum of the two other radii the force model cannot work since the triangle of Fig. 18 cannot be built up. This constraint corresponds to the forbidden area below line (D) on Fig. 10. Points in this forbidden area are nodes with a very large segment and two very thin ones. No such node is ever observed directly on the images, but a few numerical artifacts are responsible for  $R_S/R_L$  close to 1, the mean value of  $R_M/R_L$  goes down in the forbidden area. The points  $(R_M/R_L, R_S/R_L)$  are, therefore, well located in the region enclosed by the lines (A), (B), and (D). While the lines (A) and (B) are limits given by the definitions, we do not understand the origin of line (D) from the local point of view, but its absence would make the local force model collapse.

The relation between the three radii cannot be understood at this level. It rather refers to the concept of veins and hierarchy, so that a combination of global analysis and local analysis of the pattern is necessary to complete the description of its structure.

## VI. DISCUSSION AND CONCLUSION

Thus, aside from their global properties (reticulum structure and hierarchy) the leaf venations also have other common features. We have shown that the angles between vein segments are surprisingly well defined and directly related to the radii of the segments. As a simple but powerful description of this regularity in the local organization, the so-called force model has been worked out; each segment pulls on the node with a force proportional to its radius and their orientation is determined by the mechanical equilibrium. This model appropriately reproduces the measured results.

### A. The formation of the vein pattern (its ontogeny)

Focusing on the local geometry, we have introduced a local hierarchy; at each node we distinguish three segments

by their radii: the small, the intermediate, and the large one. This local hierarchy is related to the global hierarchy of veins of different orders described in the Introduction. Most of the nodes correspond to the collision of a younger vein with an older one.

The most common models (see Refs. [11–13]) for vein formation in plants assume that the differentiation results from a diffusive process. In these theories, a hormone is generated, and diffuses through the tissues, inducing a local differentiation into veins that progressively canalize the flow. In a variant of this model proposed by Meinhardt [14] the venation results from a Turing reaction-diffusion process. The simulations of both types of models lead to complex treelike branched patterns. The extremities of the branches are free; they do not reconnect to form closed loops. In this regard the morphologies differ from the observed netlike structures that are dominated by reconnections that form the reticulum.

For this reason Couder *et al.* proposed [15,16] that the venation patterns result from growth in a tensorial field. The basis of this hypothesis is that such growth naturally produces netlike morphologies. An archetype is the growth of two-dimensional (2D) crack patterns as in, e.g., drying mud or the glazes of ceramics. The origin of the formation of a reticulum is directly related to the tensorial nature of the stress field and can be easily explained. In a homogeneously 2D stretched medium the propagation of a crack relaxes one of the components of the stress. Consequently, if another crack comes from another region of the sample, it can still propagate in the vicinity of the first one by relaxing the second component of the stress. This means that, ultimately, the second crack will collide with the first one at a right angle. Couder *et al.* [15,16] performed a series of analogic experiments on the patterns generated by the drying of a gel deposited on a glass plate. Using samples of various geometries, with various boundary conditions they recovered in their experiments the main global morphologies observed in plants. In the same articles Couder *et al.* [15,16] suggested a hypothesis about a possible role of the mechanical stresses in the formation of the veins. In the initial stages of its growth a leaf is formed of two epidermal layers separated by a softer tissue; the mesophyll. It is a well known physiological fact that high stresses exist in the leaf during the growth because of the difference of these three layers. The two epidermis are under an extension stress while the mesophyll is under compression. The veins are imbedded in the mesophyll and observation of their formation shows that it occurs through successive stages. A precursor first appears when some cells differentiate into a specific tissue: the procambium. At first this procambium is only weakly differentiated from the surrounding tissue and is mainly characterized by strands of elongated cells having specific cell divisions. It is only at a later stage that the procambial cells differentiate into xylem or phloem and acquire fluid transport properties. Couder *et al.* [15,16] propose that when cells of the mesophyll are submitted to a stress larger than a threshold value they undergo specific divisions that generate the procambium.

### B. Angles in physical networks

The angles at the nodes where several fractures collide were investigated in a desiccating material by Groisman and

Kaplan [17]. They found an interesting crossover in their statistical distribution. For very thin layers the pattern is dominated by the nucleation of independent fractures around nuclei. These often have a three armed star structure and angles of  $120^\circ$  dominate the statistics. In contrast, for thicker layers, each fracture propagates on long distance and the pattern is dominated by the collisions of independent fractures at right angles. The statistical analysis of the nodes show a domination of  $90^\circ$  angles. It is worth noting, incidentally, that other networks are characterized by the angles at their nodes. For instance, in the case of 2D soap froths each node is in equilibrium; it is the point of connection of three films with an equal surface tension. The resulting angles are, therefore, always  $120^\circ$ . In the present work we undertake a similar analysis of the nodes of the leaf venation array. With the hypotheses of Couder *et al.* the venation array should have some analogy with crack patterns in that it should form a netlike pattern. However, there are also important differences. For crack patterns the formation of a fracture results in a disruption of the medium leading to a total release of the stresses. This is not the case for the proposed mechanism for the procambium formation. The stress is partially relaxed by compression of cells. Here we do not know anything about the resulting angles.

### C. Comparison with the venation network

In this paper, we established that in the venous network the angles between vein segments are surprisingly well defined. But in contrast to crack patterns and soap foams there is not a single characteristic angle, but a continuum. We have shown that this continuum results from different configurations at the nodes. The angles are directly determined by the radii of the segments. This fact can be expressed very simply by the so-called force model; each segment pulls on the node with a force proportional to its radius and their orientation is determined by the mechanical equilibrium. This model reproduces appropriately the measured results. Further, as all the studied leaves show the same behavior, the relation between the angles and the radii of the segments seems to be a universal feature in leaf venation.

The difference between the two physical networks discussed above and the venation pattern can be understood in terms of hierarchy and reorganization. Crack patterns are dominated by right angles: this results from the nonsymmetric interaction of a propagating fracture as it comes in the vicinity of a previous, frozen fracture. The interaction is limited to the time immediately preceding the fractures' collision. The resulting pattern shows a strict hierarchic organization, because the new fracture does not change the older one. In contrast, in soap foams, the characteristic  $120^\circ$  angle is due to a nonhierarchized continuous interaction; the pattern reacts instantaneously to changes and minimizes its energy, and all the forces are identical.

Here the venation pattern is an intermediate case. The veins of different order form in a sequence so that most of the nodes, like in cracks, correspond to the collision of a

younger structure with an older one. But, as in soap foams, a later mutual interaction allows a reorganization. While the veins are transported in the growth field, the growth field may not be independent of the venation pattern. Veins have mechanical properties different from the surrounding tissue. They conduct water, organic, and inorganic substances and their physiological functions can be supposed to be different. Which of these properties affect the local growth, and in which way, is not understood, but it seems evident that there is a mutual interaction between the venation pattern and growth. The measured angles and their relation to the radii can, therefore, be understood by the coexistence of local hierarchy and the possibility of reorganization.

Although we are not stating that the forces in the model are actual mechanical forces, we note that our results are compatible with the hypothesis of the role of a tensorial field in vein formation.

Accessible for mainly two-dimensional experimental investigation, leaf venation patterns can serve as a model system for network formation in biology. Such networks, neither ordered nor disordered, limited by local and global constraints, but free enough to differ from one realization to another, are current in the physical and biological worlds. Since there is a lack of methods for their characterization and a lack of understanding of their genesis, a specific study of leaf venation is more than an aesthetic pleasure.

- 
- [1] K. Esau, *Plant Anatomy* (Wiley, New York, 1953).  
 [2] K. Esau, *Vascular Differentiation in Plants* (Holt, Rinehart and Winston, New York, 1965).  
 [3] C. R. von Ettinghausen, *Die Blatt-skelette der Dykotyledonen* (Kaiserlich Königliche Hof- und Staatsdruckerei, Wien, 1861).  
 [4] L. J. Hickey, *Am. J. Bot.* **60**, 17 (1973).  
 [5] E. P. Klucking, *Leaf Venation Patterns* (J. Cramer, Berlin, 1986), Vol. 1.  
 [6] R. B. Wylie, *Am. J. Bot.* **26**, 219 (1939).  
 [7] R. B. Wylie, *Am. J. Bot.* **38**, 355 (1951).  
 [8] G. S. Avery, *Am. J. Bot.* **20**, 513 (1933).  
 [9] M. Magnasco (private communication).  
 [10] J. Munzinger, Ph.D. thesis, MNHN, Paris, 2000.  
 [11] G. J. Mitchison, *Proc. R. Soc. London, Ser. B* **207**, 79 (1980).  
 [12] R. Aloni, *Annu. Rev. Plant Physiol.* **38**, 179 (1987).  
 [13] T. Sachs, *Pattern Formation in Plant Tissues* (Cambridge University Press, Cambridge, 1991).  
 [14] H. Meinhardt, in *Positional Controls in Plant Development*, edited by W. Barlow and D. J. Carr (Cambridge University Press, Cambridge, 1984).  
 [15] Y. Couder, L. Pauchard, C. Allain, M. Adda Bedia, and S. Douady *Eur. Phys. J. B.* (to be published); <http://www.lps.ens.fr/recherche/formes/papers/veincrack.pdf>  
 [16] Y. Couder, in *Branching in Nature*, edited by V. Fleury, J. F. Gouyet, and M. Leonetti (Springer, Berlin, 2001), pp. 1–22.  
 [17] A. Groisman and E. Kaplan, *Europhys. Lett.* **25**, 415 (1994).